JOURNAL OF CATALYSIS **168,** 386–392 (1997)
ARTICLE NO. CA971644

# Relationship between the Zirconia-Promoted Reduction in the Rh-Loaded $Ce_{0.5}Zr_{0.5}O_2$ Mixed Oxide and the Zr–O Local Structure

G. Vlaic,[1,2] P. Fornasiero, S. Geremia, J. Kašpar,[2] and M. Graziani

*Dipartimento di Scienze Chimiche, Università di Trieste, Via Giorgieri 1, 34127 Trieste, Italy*

Received August 9, 1996; revised January 20, 1997; accepted January 20, 1997

**$Rh/CeO_2$–$ZrO_2$ mixed oxides show improved redox properties compared to $Rh/CeO_2$ due to a low-temperature reduction in the bulk. In the present work we have investigated the Zr–O and Ce–O local structure in $Rh/Ce_{0.5}Zr_{0.5}O_2$ by means of EXAFS and Raman spectroscopy. By introducing $Zr^{4+}$ into the $CeO_2$ lattice, the oxygen sublattice is strongly modified compared to the ideal fluorite structure of $CeO_2$: the $Ce^{4+}$ ions retain their coordination while the number of oxygens around the $Zr^{4+}$ decreases from 8 to 6 due to a displacement of two oxygens to a nonbonding distance. It is suggested that this distortion of the oxygen sublattice generates some mobile oxygens in $Rh/Ce_{0.5}Zr_{0.5}O_2$ which are responsible for the improved redox properties.** 

## INTRODUCTION

At present, all over the world, increasingly severe requirements for the abatement of exhaust gas are forced by legislation. $CeO_2$–$ZrO_2$ mixed oxides are important new materials for the automotive exhaust catalysis. Addition of $ZrO_2$ to $CeO_2$ significantly increases the thermal stability of $CeO_2$ and improves its ability to store and release oxygen (OSC) under reaction conditions (1). Both properties are of paramount importance for the development of highly efficient three-way catalysts (TWCs). To improve the catalytic efficiency during the cold start, the converter is generally located close to the engine which requires high thermal stability of the TWCs. Second, high OSC allows one to widen the operating air/fuel ratio, thereby making the catalyst less sensitive to temporary variations of A/F.

Recently, we have found an important improvement of the reduction behavior of $CeO_2$ upon formation of mixed $CeO_2$–$ZrO_2$ oxides (2). We have observed that in Rh-loaded $Ce_{1-x}Zr_xO_2$ ($x = 0.1$–$0.9$), the addition of an increasing amount of $ZrO_2$ lowers the temperature of the reduction of $Ce^{4+}$ in the bulk, reaching a minimum of 600 K for the cubic $Rh/Ce_{0.5}Zr_{0.5}O_2$. This value is about 500 K lower than the temperature of reduction in the bulk of $Rh/CeO_2$. The ability of $Rh/Ce_{0.5}Zr_{0.5}O_2$ to undergo reduction in the bulk at such a low temperature results in an unusually high oxygen exchange capacity of this support. We have attributed this enhancement of the reducibility to an increased oxygen mobility in the bulk induced by the addition of the Zr into the $CeO_2$ lattice (2) which gives unusual redox properties to these systems (3).

Efficient redox catalysts have a large impact on environmental catalysis because of their extensive use in the oxidative removal of volatile organic compounds, in catalytic combustors and TWCs. In this respect, we recently reported the crucial role of bulk oxygen vacancies in promoting the catalytic removal of NO by its reaction with CO using the above Rh- and Pt-loaded mixed oxides as catalysts (4). The $Ce^{3+}/Ce^{4+}$ redox couple was indeed shown to efficiently reduce NO, suggesting the feasibility of new-generation Rh-free TWC. High oxygen mobility in the bulk was also recognized to be responsible for the high activity in the oxidation reactions of $CeO_2$-containing mixed oxides (5, 6).

While extensive evidence is available for the important role of $ZrO_2$ in modifying the redox and catalytic behavior of the $CeO_2$, up to date, there is no direct experimental evidence as to how the structural modification of the $CeO_2$ induced by the presence of $ZrO_2$ may be correlated to the above behavior.

In order to understand the role of the addition of $ZrO_2$ in modifying the redox properties, we are carrying out a systematic investigation of the local structure of the above Rh-containing solid solutions. Here we report the results obtained for the cubic $Rh/Ce_{0.5}Zr_{0.5}O_2$ which, as reported above, represents the best composition for obtaining a highly efficient redox system. The main point addressed is the modification of the oxygen distribution around the metal center in order to understand how it can influence the oxygen mobility. Second, we wished to ascertain the homogeneity at the atomic level of a $CeO_2$–$ZrO_2$ solid solution which is still a matter of debate (7, 8).

[1] Also Sincrotrone Trieste, Padriciano 99, 34100 Trieste, Italy.
[2] To whom correspondence should be addressed. Fax: +39-40-6763903.



0021-9517/97 $25.00

## EXPERIMENTAL

### *Materials*

The catalysts were the same as in previous studies (2, 4). In short, the preparation is carried out as follows. The cubic $Ce_{0.5}Zr_{0.5}O_2$ was prepared by firing at 1873 K a mixture of oxides of appropriate composition which was then quenched to room temperature. This yielded a product whose powder XRD spectrum was indexed (2) according to Ref. (9) in the cubic $Fm3m$ space group. A lattice parameter of 5.274 Å was evaluated. An average M−O distance of 2.30 Å was calculated assuming that the oxygen atoms are located in the tetrahedral sites of the fluorite structure. The support was Rh-loaded (0.5% wt) by incipient wetness.

### *EXAFS Spectra*

*Experimental procedure.* For the measurements at the Zr $K$ edge, finely grounded weighed amounts (≈50 mg) of the powders were pressed in thin self-supporting pellets of an approximate diameter of 1 cm. For measurements at the Ce $L_{III}$ edge, the powder (5–8 mg) was deposited from an acetone suspension on a graphite holder. The amount of sample was calculated to obtain a total absorption coefficient ($\mu x$) after the edge jump of about 2.5. Sample homogeneity was carefully controlled by photographic methods and using an optical microscope. Spectra of Zr (metal), $m$-$ZrO_2$, $BaZrO_3$, and $CeO_2$ were collected as reference compounds.

The measurements were performed in transmission mode at room temperature on the EXAFS-I line at the DCI storage ring (1.85 GeV, 300 mA) at Lure (Orsay, France), using a channel-cut Si (331) monochromator. The incident and transmitted photon flux was measured using two ionization chambers, the first filled with air and the second with argon or air for Zr and Ce, respectively. The absence of any contribution to the spectrum of photons due to the third harmonic of the Ce $L_{III}$ edge was accurately checked. The energy scale was calibrated with a copper foil by attributing the value of 8991.1 eV at the first maximum after the edge jump. At least three scans were recorded for each sample in the energy interval 17,900–18,900 eV for the Zr $K$ and 5670–6160 for the Ce $L_{III}$ edge, respectively, using steps of 2 eV. Each point was measured for 2 s and the dimensions of the beam were approximately $2 \times 6$ mm.

*Data analysis.* The EXAFS spectra were analyzed according to standard procedures (10) using a program set written by Michalowicz (11). The final signals which are shown in Fig. 1 were obtained by averaging the three individual EXAFS data. The standard deviations were calculated point by point as a measure of the experimental errors in the final functions. Following the recommended procedures described by the International Workshop on Standards and Criteria in XAFS (12, 13), to obtain the structural parameters, we fitted the Fourier filtered data in $k$-space. The EXAFS signals multiplied by $k^3$ were then Fourier transformed in the limits 3.05–12.70 $Å^{-1}$ for Zr and 2.40–9.85 $Å^{-1}$ for Ce. The peaks present in $R$ space were then back-transformed to $k$ space. To model the first peak, we measured the EXAFS signals and deduced phases and amplitudes from $BaZrO_3$ and $CeO_2$ for Zr−O and Ce−O, respectively. For more distant shells we used the McKale functions (14), after their testing on reference samples of known structure ($m$-$ZrO_2$, Zr, $CeO_2$, $BaZrO_3$) to evaluate the photoelectron mean free path.

In all the fits, the number of free parameters $N_{par}$ was kept smaller than the number of independent points $N_{ind}$, defined as

$$N_{ind} = 2\Delta R \Delta k/\pi$$

($\Delta R$ is the width of the $R$-space filter windows, and $\Delta k$ is the actual interval of the fit in the $k$ space).

The goodness of the fit was discriminated by using the reduced $\chi^2$ term $\varepsilon_\nu^2$, as defined in Refs. (15, 16), where $\nu$ is the degree of freedom ($\nu = N_{ind} - N_{par}$). When the model used for the fit, and the standard deviation of the filtered points, is properly evaluated, $\varepsilon_\nu^2$ must approach unity. The error bars of the parameters were evaluated by stepping each parameter, while optimizing the others, until $\varepsilon^2$ increases by 1 above its minimum value. As suggested by Refs. (15, 16) we used the $F$ test (17) to determine, when necessary, whether the change in $\varepsilon_\nu^2$ is statistically significant when an extra parameter is added or the model is changed. It should be noted that while a wrong choice of standard deviation has an influence on the $\varepsilon_\nu^2$ value, it is canceled in the $F$ test.

### *XRD and FT Raman Spectra*

Powder X-ray diffraction patterns were collected on a Siemens Kristalloflex Mod.F Instrument (Ni-filtered Cu$K\alpha$). Cell parameters were determined by using the TREOR90 program which employs the Visser algorithm. The peak deconvolution was carried out after subtraction of the contribution of the $K\alpha_2$ line to the spectrum. Pearson VII functions were employed for the peak deconvolution.

FT Raman spectra were measured on a Perkin Elmer 2000 FT Raman spectrometer with a diode-pumped YAG laser and a room-temperature super InGaAs detector. The laser power was 50–200 mW.

## RESULTS AND DISCUSSION

Figure 2a reports the modulus of the Fourier transform of the EXAFS signal of the $Rh/Ce_{0.5}Zr_{0.5}O_2$ sample measured at the Zr $K$ edge. The region 1.11–2.34 Å is associated with the Zr−O bonding while the region 2.35–4.12 Å is mainly associated with the Zr–$M$ ($M$ = Zr, Ce) interactions. For the modeling of the first peak, we have employed the experimental phase and amplitude deduced

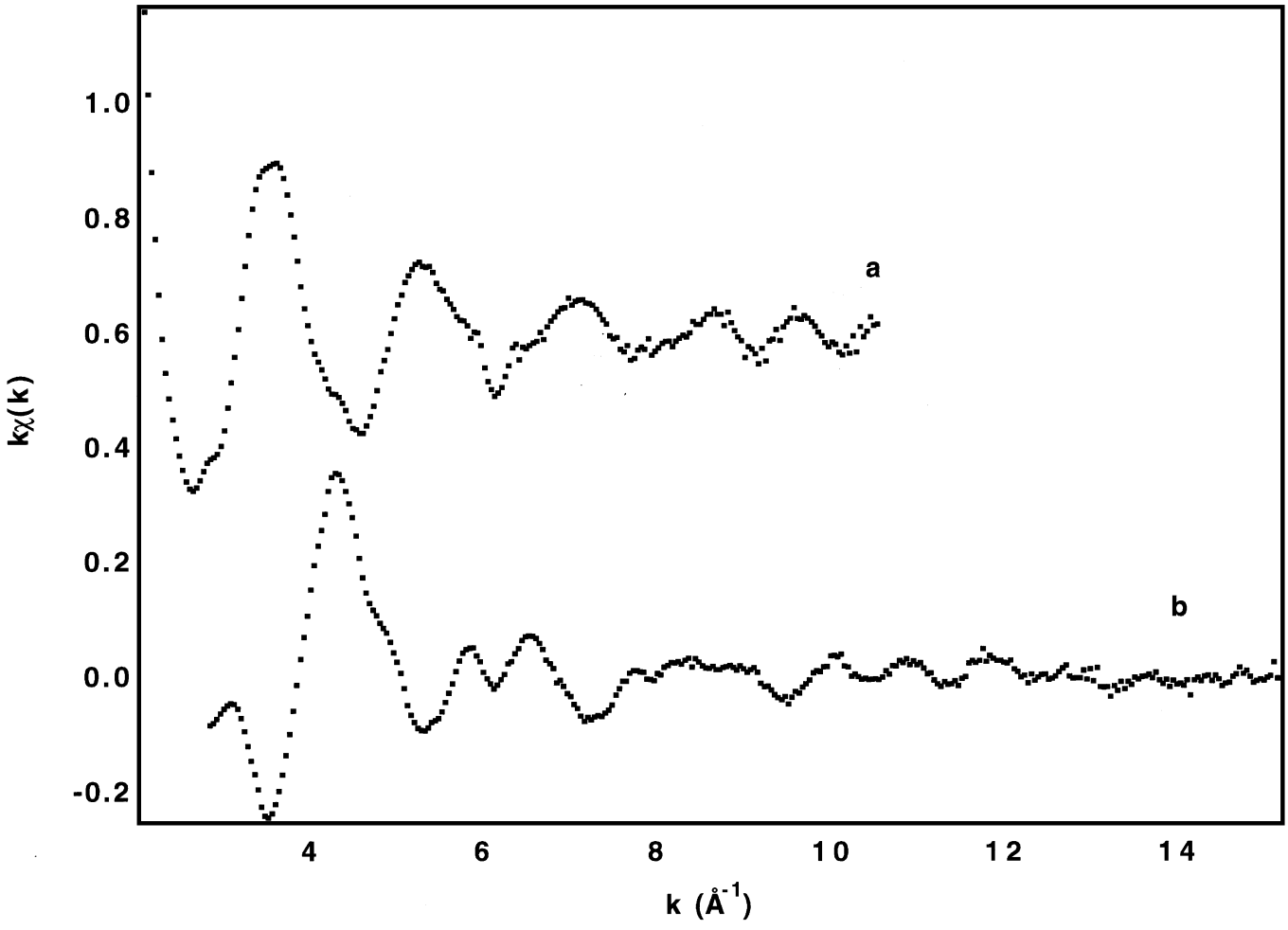


**FIG. 1.** Experimental EXAFS spectra as $k\chi(k)$ vs $k$ of (a) $L_{III}$ edge of Ce and (b) $K$ edge of Zr of $Rh/Ce_{0.5}Zr_{0.5}O_2$. For the sake of clarity, spectrum (a) is displaced by 0.6 $k\chi(k)$.

from $BaZrO_3$. The following $BaZrO_3$ structural data were used: $R$ (Zr–O) = 2.09 Å, coordination number (C.N.) = 6, and $\sigma = 0.07$ Å (18). $CeO_2$ has the fluorite structure with eight oxygens as nearest neighbors (NN) located in the tetrahedral sites at a distance of 2.34 Å. $ZrO_2$ is monoclinic ($m$) at room temperature; however, the tetragonal ($t$) and cubic ($c$) phases can be stabilized at room temperature upon addition of dopants. Three different local structures were reported for the $M$–O shell in $c$-$ZrO_2$: a single shell of eight Zr–O bonds and two each with two subshells with $4+4$ or $6+2$ oxygens, respectively, at a short (Zr–O = 2.07–2.14) and long (Zr–O = 2.34–2.42) distance from Zr (19).

The reliability of a total of 40 different models using up to three oxygen subshells with C.N. 6–8 has been examined. Interatomic distances, coordination numbers, and Debye–Waller factors were allowed to vary in the preliminary fits, while for the final fits we kept the C.N. fixed for most of the cases (Table 1). For the sake of comparison, the results obtained for a few significant models among the above-quoted 40 ones are included in Table 1. A perusal of these models and the application of the $F$ test reveal that the two-subshell model (C.N. = 4 + 2) reported in Table 1 gives the best fit of the experimental data with a reliability of at least 75%. The goodness of the fit is illustrated in Fig. 2b. In addition to the statistical consideration, it should be recalled that the other models show some physically unreliable values such as the Debye–Waller factor. The observed C.N. = 4 + 2 means that the two "missing" oxygens are at a distance Zr–O $\geq$ 2.60 Å. It is important to note at this point that when the single-shell model is used for the fitting, by allowing the C.N. to vary, a final value of C.N. = 4.3 and a $\sigma = 0.103$ Å are obtained (Table 1). These values are consistent with a strong contribution of the C.N. = 4 subshell to the FT of the EXAFS signal in the region 1.11–2.34 Å supporting the C.N. = 4 + 2 model. Attempts have been made to localize these "missing" oxygens using three-shell models. The only one (C.N. = 4 + 2 + 2; degree of freedom = 1) which is acceptable on the basis of the $F$ test is reported

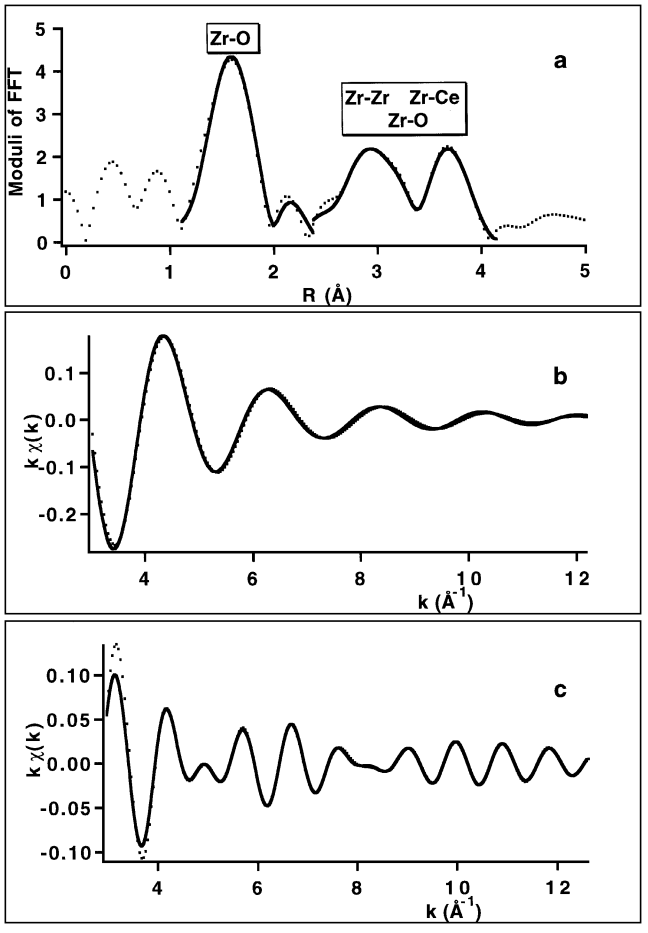


**FIG. 2.** (a) Modulus of the Fourier transform (FT) of the experimental data and the modeled FTs relative to the first and second shell ($R$ space); (b) back-FT of the first peak and the corresponding fit; (c) back-FT of the second peak and the corresponding fit ($k$ space). (■) Experimental, (—) fit.

in Table 1. However, it should be noted that the values $\sigma = 0.214$ Å and $\Delta R = 0.20$ are very large. In our interpretation, this is an indication of a high disorder (static and thermal) which makes the contribution of these oxygens to the EXAFS signal very small and difficult to evaluate. In accordance, preliminary experiments carried out at liquid He temperature confirm the validity of the $4 + 2$ model.

Since the coordination number and the Debye–Waller factors ($\sigma$) are correlated, in order to verify the internal consistency of the fitting we also allowed the C.N. to float (Table 1). In this fit the $\Delta E$ were kept constant in order to satisfy the above limitations on $N_{\text{ind}}$. Significantly, neither the Debye–Waller factors nor the C.N. change appreciably which further substantiates the observation that the $Zr^{4+}$ inserted in the $CeO_2$ lattice favors a displacement of the NN oxygens, decreasing its C.N. Consistent with our observation, examination of cubic $ZrO_2$ stabilized with $Y^{3+}$ suggested that the oxygen vacancies are located at the $Zr^{4+}$, decreasing the C.N. to 7 (20).

The analysis of Ce–O NN local structure was performed on the back-FFT in the range 1.14–2.43 Å. It was carried out in the same way as reported for the Zr $K$ edge, e.g., keeping the C.N. constant in the final fits. A fit using a single-shell model and varying the C.N. is also included in Table 1. As shown in Fig. 3a, an excellent agreement is observed between the experimental data and the modeled data on the basis of a single-shell model with C.N. = 8. This is in contrast to the results observed at the Zr $K$ edge, suggesting that the Ce ions maintain the coordination as in $CeO_2$.

The model proposed for the modification of the oxygen sublattice induced by the presence of $ZrO_2$ is further supported by the Raman spectra (Fig. 4). Six Raman-active modes of $A_{1g} + 3E_g + 2B_{1g}$ symmetry are observed for tetragonal $ZrO_2$ (space group $P4_2/nmc$), while for the cubic fluorite structure (space group $Fm3m$) only one $F_{2g}$ mode centered at around 490 $cm^{-1}$ is Raman-active (21). In pure $CeO_2$, which also has the fluorite structure, the $F_{2g}$ mode is observed at 465 $cm^{-1}$. Accordingly, we find a

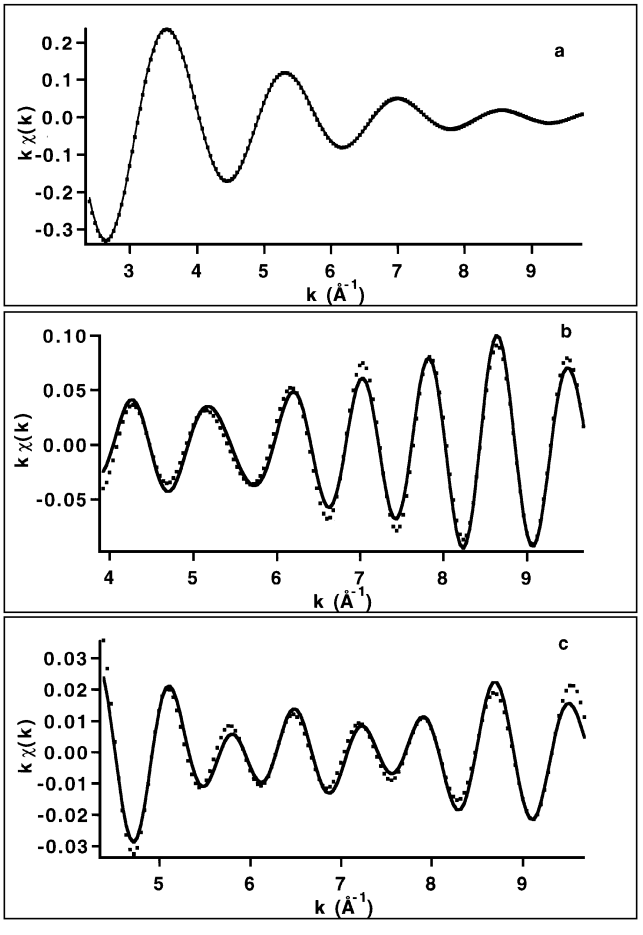


**FIG. 3.** (a) Back-FT of the first peak and the corresponding fit at the Ce $L_{\text{III}}$ edge of $Ce_{0.5}Zr_{0.5}O_2$; (b) back-FT of the second peak and the corresponding fit at the Ce $L_{\text{III}}$ edge of $CeO_2$; (c) back-FT of the second peak and the corresponding fit at the Ce $L_{\text{III}}$ edge of $Ce_{0.5}Zr_{0.5}O_2$ ($k$ space). (■) Experimental, (—) fit.

**TABLE 1**

**Local Coordination in $Ce_{0.5}Zr_{0.5}O_2$ as Determined from EXAFS Measured at Zr *K* and Ce $L_{III}$ Edges**

| | | C.N.[a] | *R* (Å) | $\sigma$ (Å) | $\Delta E$ (eV) | $\nu$ | $\varepsilon_\nu^2$ |
|---|---|---|---|---|---|---|---|
| Zr *K* edge | | | | | | | |
| I shell | Zr–O | 8 | 2.113 ± 0.007 | 0.142 ± 0.010 | −3.4 ± 0.6 | 4 | 21.2 |
| | | 4.3[b] | 2.104 ± 0.005 | 0.103 ± 0.010 | −4.0 ± 0.6 | 3 | 7.0 |
| | | 4 | 2.130 ± 0.006 | 0.073 ± 0.004[c] | 5.2 ± 0.6 | 3 | 36.4 |
| | | 4 | 2.339 ± 0.007 | | | | |
| | | 6 | 2.130 ± 0.007 | 0.110 ± 0.001[c] | −1.0 ± 0.7 | 3 | 7.6 |
| | | 2 | 2.360 ± 0.016 | | | | |
| | | 4 | 2.115 ± 0.008 | 0.078 ± 0.003[c] | 0.0 ± 0.5 | 3 | 1.9 |
| | | 2 | 2.324 ± 0.011 | | | | |
| | | 4 | 2.112 ± 0.008 | 0.079 ± 0.003[c] | −0.5 ± 1.0 | 1 | 3.6 |
| | | 2 | 2.318 ± 0.014 | | | | |
| | | 2 | 2.60 ± 0.20 | 0.214 ± 0.068 | | | |
| | | 3.8 ± 0.3[b] | 2.112 ± 0.003 | 0.079 ± 0.006 | 0[a] | 1 | 3.6 |
| | | 1.9 ± 0.3[b] | 2.311 ± 0.008 | 0.080 ± 0.010 | | | |
| II shell | Zr–Zr | 6 | 3.64 ± 0.04 | 0.105 ± 0.006 | −10.7 ± 4.7 | 1 | 0.9 |
| | Zr–Ce | 6 | 3.72 ± 0.01 | 0.095 ± 0.007 | −6.8 ± 1.5 | | |
| | Zr–O | 24 | 4.24 ± 0.03 | 0.140 ± 0.010 | −8.3 ± 2.0 | | |
| Ce $L_{III}$ edge | | | | | | | |
| I shell | Ce–O | 8 | 2.312 ± 0.007 | 0.092 ± 0.005 | −0.3 ± 0.3 | 3 | 0.6 |
| | | 7.6 ± 0.4 | 2.308 ± 0.008 | 0.085 ± 0.009 | −0.5 ± 0.4 | 2 | 0.4 |
| II shell | Ce–Zr | 6 | 3.75 ± 0.03 | 0.106 ± 0.08 | 15 ± 4 | 1 | 0.9 |
| | Ce–Ce | 6 | 3.72 ± 0.01 | 0.095 ± 0.007 | −6.8 ± 1.5 | | |
| | Zr–O | 24 | 4.50[a] | 0.086 ± 0.025 | 14[a] | | |

[a] Values were kept constant in the fitting.
[b] C.N., coordination number, is allowed to vary in the fitting.
[c] The same values of $\sigma$ were employed for the two subshells.

single band at 465 $cm^{-1}$ for pure $Rh/CeO_2$, while six bands at 140, 246, 313, 456, 574, and 622 $cm^{-1}$ are observed for $Rh/Ce_{0.2}Zr_{0.8}O_2$. As detected by XRD (2), the latter sample is a tetragonal phase for which a C.N. (Zr–O) = 4 + 4 (space group $P4_2/nmc$) was observed (19, 20). Our preliminary results of the EXAFS characterization of this sample are in accord with such a Zr–O coordination. The observation of only four bands in the $Rh/Ce_{0.5}Zr_{0.5}O_2$ sample clearly supports the results of the EXAFS analysis, suggesting that both C.N. = 8 and C.N. = 4 + 4 models should be rejected. It should be noted that the $F_{2g}$ mode due to the symmetrical stretching of the Ce–O bond would shift toward higher frequencies as a result of the contraction of the cell parameter due to introduction of the smaller $Zr^{4+}$ (ionic radii: 0.97 Å, $Ce^{4+}$ vs 0.84 Å, $Zr^{4+}$). For the modeling of the peaks at 2.35–4.12 Å (Zr, *K* edge, Fig. 2a), we employed the theoretical phases and amplitudes reported by McKale after testing their reliability on model compounds (Zr metal, $BaZrO_3$, *m*-$ZrO_2$). It is important to note that this region cannot be modeled with a Zr–Zr shell only. Use of Zr–Zr and Zr–Ce subshells with C.N. = 6 for each shell is necessary to obtain a reasonable fit. These C.N.'s are consistent with the composition of the sample, suggesting that a homogeneous solid solution is formed. Inclusion of a Zr–O subshell further improves the quality of the fit at low *k* range. The optimized parameters are reported in Table 1.

The validity of all the fits at the Zr *K* edge is confirmed in Fig. 2 which shows an excellent agreement of the experimental data and the model in both *R* and *k* space. The consistency of the results of fitting at the Zr *K* edge with those obtained at the Ce $L_{III}$ edge was also checked (Table 1). The analysis was performed on the back-FT in the range 2.46–4.68 Å. It should be noted that modeling of the EXAFS signal at the Ce $L_{III}$ edge presents intrinsic difficulties since only a short energy range is available due to the appearance of the Ce $L_{II}$ edge. Moreover, the unavailability of models for the Ce–Zr bond precluded the use of experimental phases and amplitudes for the fitting of the second shell.

The use of the McKale functions for the next nearest neighbors (NNN) showed somewhat less good agreement for $CeO_2$ (Fig. 3b) compared to $ZrO_2$. A quite reasonable agreement, however, is obtained for the Ce–Ce bond: 3.80 Å vs 3.82 Å measured by XRD. A less accurate definition of the Ce $L_{III}$ edge phases and amplitude given by McKale *et al.* cannot be excluded as the cause of the poorer agreement observed for the Ce $L_{III}$ edge compared to the Zr *K* edge. For example, the polarizability, which was not taken into account in their model (14), is

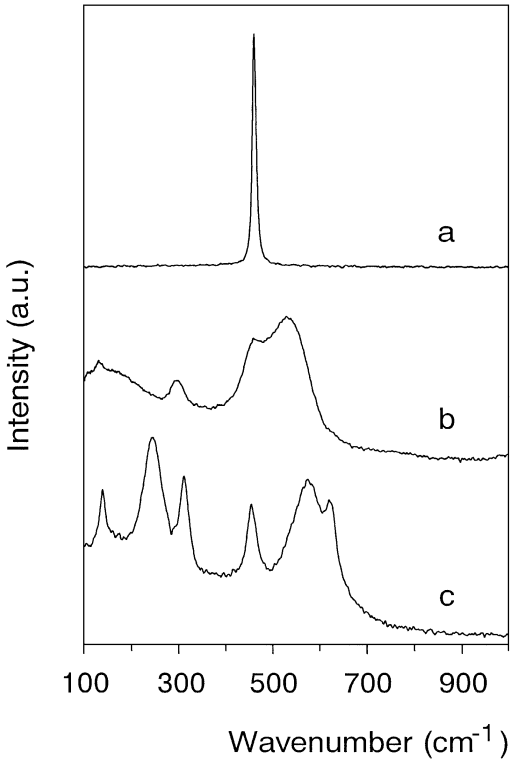


**FIG. 4.** Raman spectra of (a) $CeO_2$, (b) $Ce_{0.5}Zr_{0.5}O_2$, and (c) $Ce_{0.2}Zr_{0.8}O_2$.

considerably higher for $Ce^{4+}$ than for $Zr^{4+}$. The Ce–O bond (II shell) is overestimated by 0.10 Å using the McKale functions: 4.58 Å vs 4.48 Å measured by XRD. Consequently, due to the short energy interval, we kept constant the values concerning the Ce–O contribution for modeling $Rh/Ce_{0.5}Zr_{0.5}O_2$. A $R$ (Ce–O) = 4.50 Å was used to take the contraction of the cell parameter into account (5.407 and 5.374 Å, respectively, for $CeO_2$ and $Ce_{0.5}Zr_{0.5}O_2$). There is satisfactorily agreement of the modeled and experimental data for the NNN at the Ce $L_{III}$ edge as shown in Fig. 3c. The consistency of the lengths of the Ce–Zr bonds with those obtained at the Zr $K$ edge clearly supports the entire analysis.

A possible structural model for the $Ce_{0.5}Zr_{0.5}O_2$ mixed oxide which rationalizes the results of the fitting of the EXAFS data is illustrated in Fig. 5. In this model which is derived from the $CeO_2$ structure, $Ce^{4+}$ and $Zr^{4+}$ alternatively occupy the corner and the face centered positions of the fcc unit cell. With such a site occupancy, the $Zr^{4+}$ has on average 6 $Ce^{4+}$ and 6 $Zr^{4+}$ as NNN, while the oxygens present two different local structures (Fig. 5): type A oxygens have 3 $Ce^{4+}$ and 1 $Zr^{4+}$ as NN; type B oxygens have 1 $Ce^{4+}$ and 3 $Zr^{4+}$ as NN. With respect to $CeO_2$, for type A oxygens only 1 $Zr^{4+}$ is substituted for $Ce^{4+}$ and therefore no strong perturbation of the local structure can be expected. We associate the Zr–O = 2.324 Å bond to this situation which is very close to the Ce–O = 2.31 Å bond. For type B oxygens, 3 of 4 $Zr^{4+}$ are substituted for $Ce^{4+}$. In such a situation a strong distortion of the oxygen sublattice can be expected. The oxygen moves close to two of the three neighboring $Zr^{4+}$ ions (Zr–O = 2.13 Å), keeping the length of the Ce–O bond constant at 2.31 Å. Consequently, one of the Zr–O bonds is elongated ($\geq$2.60 Å) and it is no longer detected in the first shell of Zr. As a result, every $Ce^{4+}$ remains bonded to 8 oxygen atoms at 2.31 Å. In the case of $Zr^{4+}$, there are two type A (Zr–O = 2.34 Å) and six type B oxygens as NN. Of these, four come close (Zr–O = 2.13 Å) and two are pushed away (Zr–O $\geq$ 2.60 Å).

At present, some points appear evident from this work. The overall picture strongly suggests that the structural modifications due to addition of $ZrO_2$ to the $CeO_2$ lattice are responsible for the unusual promotion of the reduction in the bulk of the $CeO_2$–$ZrO_2$ solid solutions. The contraction of the cell parameter, due to the substitution of the $Ce^{4+}$ (0.97 Å) with the smaller $Zr^{4+}$ (0.84 Å), and the tendency of Zr–O to retain the typical Zr–O bond distances favor a decrease of the C.N. of the $Zr^{4+}$ from 8 such as in $c$-$ZrO_2$ to 6. The fact that two oxygens are pushed away from the $Zr^{4+}$ to a nonbonding distance longer than 2.60 Å suggests a large lability. Further work, however, is necessary to assess the general validity of such a model.

A remaining question is whether such an oxygen configuration survives the oxygen ion transport in the reduction/oxidation processes without relaxation. As shown in our recent paper on a high surface area $Ce_{0.5}Zr_{0.5}O_2$, redox cycles carried out up to 1273 K caused distortions of the oxygen sublattice which resulted in a shift of the reduction

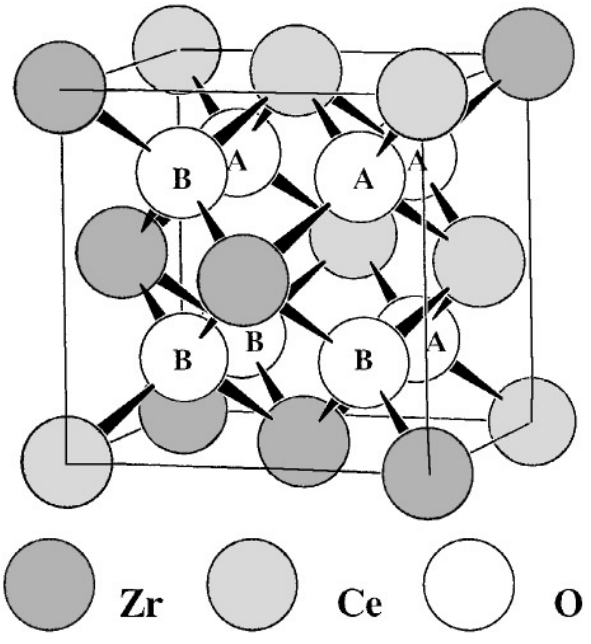


**FIG. 5.** A possible structural model of the fcc unit cell of $Ce_{0.5}Zr_{0.5}O_2$.

in the bulk of the solid solution to low temperatures (3, 22). This confirms a direct relationship between the two effects.

Summarizing, the present work shows that properly designed structural modification of the $CeO_2$ may lead to floating oxygens in the lattice which effectively enhance the redox properties of these catalytically interesting materials.

Finally, it is confirmed that a truly homogenous $Ce_{0.5}Zr_{0.5}O_2$ solid solution may be formed which avoids the formation of a domain-type structure when an appropriate method of synthesis is adopted. This is an important observation in view of the efforts to develop methodologies for the synthesis of these important materials (23).

## ACKNOWLEDGMENTS

Ministero dell'Università e della Ricerca Scientifica (MURST 40% and 60%), Università di Trieste, and EU Large Installation Program are acknowledged for financial support.

## REFERENCES

1. Eur. Pat., EP 337809, Appl. 18/10/1989; Ger. Offen., DE 37377419, Appl. 19/5/1988.
2. Fornasiero, P., Di Monte, R., Ranga Rao, G., Kašpar, J., Meriani, S., Trovarelli, A., and Graziani, M., *J. Catal.* **151**, 168 (1995).
3. Balducci, G., Fornasiero, P., Di Monte, R., Kašpar, J., Meriani, S., and Graziani, M., *Catal. Lett.* **33**, 193 (1995).
4. Ranga Rao, G., Fornasiero, P., Di Monte, R., Kašpar, J., Vlaic, G., Balducci, G., Meriani, S., Gubitosa, G., Cremona, A., and Graziani, M., *J. Catal.* **162**, 1 (1996).
5. Zamar, F., Trovarelli, A., de Leitenburg, C., and Dolcetti, G., *J. Chem. Soc. Chem. Commun.*, 965 (1995).
6. Tschope, A., Liu, W., Flytzanistephanopoulos, M., and Ying, J. Y., *J. Catal.* **157**, 42 (1995).
7. Voronko, Y. K., Sobol, A. A., Ushakov, V. A., and Tsymbal, L. Y., *Inorg. Mater.* **30**, 747 (1994).
8. Hirata, T., Asari, E., and Kitajima, M., *J. Solid State Chem.* **110**, 201 (1994).
9. Meriani, S., and Spinolo, G., *Powder Diffract.* **2**, 255 (1987).
10. Lee, P. A., Citrin, P. H., Eisenberg, P., and Kincaid, B., *Rev. Mod. Phys.* **53**, 769 (1981).
11. Michalowicz, A., "Logiciel pour la Chimie," p. 102. Societé Francaise de Chimie, Paris, 1991.
12. Lytle, F. W., Sayers, D. E., and Stern, E. A., *Physica B* **158**, 701 (1989).
13. Hasnain, S. S. (Ed.), "X-Ray Adsorption Fine Structure," pp. 752–770. Ellis Horwood, New York, 1991.
14. McKale, A. G., Veal, B. W., Paulikas, A. P., Shaw, S. K., and Knapp, G. J., *J. Am. Chem. Soc.* **110**, 3763 (1988).
15. Joyner, R. W., Martin, K. J., and Meehan, P., *J. Phys. C: Solid State Phys.* **20**, 4005 (1987).
16. Freund, J., *Phys. Lett. A* **157**, 256 (1991).
17. Bevington, R. P., and Robinson, D. K., "Data Reduction and Error Analysis for the Physical Sciences," 2nd ed., Chap. 11. McGraw–Hill, New York, 1992.
18. Vlaic, G., Navarra, G., Regnard, J.-R., Williams, C. E., and Jérome, R., *J. Phys. II Fr.* **5**, 665 (1995).
19. Horward, C. J., Hill, R. J., and Reichert, B. E., *Acta Crystallogr. B: Struct. Sci.* **44**, 116 (1988).
20. Li, P., Chen, I. W., and Penner-Hahn, J. E., *Phys. Rev. B* **48**, 10063 (1993).
21. Keramidis, V. G., and White, W. B., *J. Am. Ceram. Soc.* **57**, 22 (1974).
22. Fornasiero, P., Balducci, G., Di Monte, R., Kašpar, J., Sergo, V., Gubitosa, G., Ferrero, A., Graziani, M., *J. Catal.* **164**, 173 (1996).
23. de Leitenburg, C., Trovarelli, A., Zamar, F., Maschio, S., Dolcetti, G., and Llorca, J., *J. Chem. Soc. Chem. Commun.*, 2181 (1995).